inorganics

MDPI

Article

Facile Construction of $Bi_2Sn_2O_7$/g-C_3N_4 Heterojunction with Enhanced Photocatalytic Degradation of Norfloxacin

Zhengru Zhu [1], Haiwen Xia [1], Hong Li [2,*] and Songlin Han [1]

[1] School of Geography, Liaoning Normal University, Dalian 116029, China
[2] Department of Basic, Dalian Naval Academy, Dalian 116018, China
* Correspondence: lswlx903@163.com

Abstract: To mitigate antibiotic residues in the water environment, $Bi_2Sn_2O_7$/g-C_3N_4 (BSCN) heterojunction was fabricated by a facile ultrasound-assisted hydrothermal method. The microstructure, morphology, and optical properties of $Bi_2Sn_2O_7$/g-C_3N_4 heterojunction was studied by XRD, FTIR, XPS, SEM, TEM, UV–Vis DRS, and PL. The degradation rate of 20 mg/L norfloxacin (NOR) under visible light for 3 h was adopted as one of the indexes to evaluate the photocatalytic performance of $Bi_2Sn_2O_7$/g-C_3N_4 heterojunction. Embellished with 20% $Bi_2Sn_2O_7$ (BSO), the $Bi_2Sn_2O_7$/g-C_3N_4 heterojunction decomposed 94% NOR in the experimental solution, which was 2.35 and 3.03 times as much as pristine g-C_3N_4 and bare $Bi_2Sn_2O_7$, respectively. In addition, the $Bi_2Sn_2O_7$/g-C_3N_4 heterojunction still eliminated 89% of NOR after five cycles, portending outstanding stability and cyclability of photocatalytic activity. A possible photocatalytic mechanism of $Bi_2Sn_2O_7$/g-C_3N_4 heterojunction for NOR degradation is proposed.

Keywords: $Bi_2Sn_2O_7$/g-C_3N_4; heterojunction; photocatalyst; norfloxacin; water pollution control

Citation: Zhu, Z.; Xia, H.; Li, H.; Han, S. Facile Construction of $Bi_2Sn_2O_7$/g-C_3N_4 Heterojunction with Enhanced Photocatalytic Degradation of Norfloxacin. *Inorganics* **2022**, *10*, 131. https://doi.org/10.3390/inorganics10090131

Academic Editors: Duncan H. Gregory, Wolfgang Linert, Richard Dronskowski, Vladimir Arion, Claudio Pettinari and Torben R. Jensen

Received: 18 July 2022
Accepted: 31 August 2022
Published: 1 September 2022

1. Introduction

Antibiotic as an efficacious treatment method in human and veterinary bacterial infection has lasted decades years [1]. However, antibiotics cannot be completely decomposed in organisms, and the residue is excreted as an aqueous solution, further, back to the water environment with the discharge of sewage [2]. The existing remediation technologies of polluted water cannot remove antibiotics completely [3]. According to previous reports, more than 100,000 tons of antibiotics is consumed globally every year, including NOR, a fluoroquinolone antibiotic that has been widely applied and frequently detected in natural water bodies, even in the drinking water of humans, posing a serious threat to human health [4,5]. Clearly, it is urgent to put forward an efficient, inexpensive, and environment-friendly water-pollution treatment method.

With the advantage of simple steps, high efficiency and little secondary pollution, semiconductor photocatalysis technology has gained increasing interest regarding the treatment of polluted water [6,7]. Photocatalysts generate photoinduced electrons and holes on the surface when exposed to the light with sufficient energy. These photogenerated electron holes then transform water and oxygen in the water to produce the active substances superoxide and hydroxyl radicals [8]. Pollutants in water will also be broken down by these active substances into CO_2, H_2O, and other harmless products [9]. However, traditional photocatalysts are only UV light active (about 4% of sunlight), as they have a wide bandgap, for example, TiO_2 (~3.2 eV) [10] and ZnO (~3.3 eV) [11], thus limiting their practical application [12]. Most of the energy from sunlight cannot be utilized by these wide-bandgap photocatalysts. Thus, how to take advantage of the full spectrum of solar light is a much more meaningful but challenging research subject. Fortunately, a series of visible-light-driven photocatalysts have come out in recent years, such as $LaFeO_3$ [13], Bi_2WO_6 [14], $BiVO_4$ [15], etc. The emergence of photocatalysts driven

by visible light holds promise for the treatment of antibiotic residues in the water environment.

Graphite-phase carbon nitride (g-C_3N_4, abbreviated as CN) is a non-metallic polymeric semiconductor that was first applied to photocatalysis in 2009 by Wang and his co-workers [16]. Due to the advantage of inexpensive cost, controllable morphology, stable chemical properties, and visible-light response ability, CN has attracted extensive attention in recent years [17]. However, drawbacks have been exposed gradually in the process of further research, such as rapid photogenerated carrier recombination, small specific surface area, and so on [18]. The construction of heterojunction photocatalyst is one of the ideal methods to solve the above problems; for example, Sun et al. [19] synthesized a Z-scheme BiOCl/g-C_3N_4 heterojunction and decomposed 97.1% tetracycline within 60 min. Hu et al. [20] doped g-C_3N_4 with TiO_2 to degrade ciprofloxacin, and the degradation rate achieved 93.4% in 60 min, which is 2.3 and 7.5 times higher than TiO_2 and g-C_3N_4. Zhang et al. [21] embellished g-C_3N_4 with $NaNbO_3$ to disintegrate ofloxacin, and the degradation reached 99.5% within 30 min, whereas monomer $NaNbO_3$ and g-C_3N_4 can only eliminate 42.5% and 21.1% of ofloxacin under the same conditions.

$Bi_2Sn_2O_7$ is also a photocatalyst that can respond to visible light [22]. With a corner-shared octahedral network, it is easier for photogenerated electrons to migrate on the surface of $Bi_2Sn_2O_7$, which benefits the separation efficiency of photogenerated electrons and holes [23]. Thus, $Bi_2Sn_2O_7$ seems to be an ideal partner of g-C_3N_4. Previously, $Bi_2Sn_2O_7$/g-C_3N_4 photocatalysts have been demonstrated to be effective in degrading dyes such as rhodamine B (Rhb), methylene blue (MB), and acid red 18 (AR 18) [24,25]. Few research studies have been performed on the degradation of antibiotics [26].

Hence, $Bi_2Sn_2O_7$/g-C_3N_4 heterojunction photocatalysts with different dosages of BSO (10%, 20%, 30%, 40%, and 50%, denoted as 10BSCN, 20BSCN, 30BSCN, 40BSCN, and 50BSCN) were synthesized by a facile ultrasound-assisted hydrothermal method and characterized by XRD, FTIR, XPS, SEM, TEM, UV–Vis DRS, and PL. NOR was selected as the degradation target to evaluate the photocatalytic performance of heterojunction photocatalyst under visible light. Ultimately, a possible mechanism of $Bi_2Sn_2O_7$/g-C_3N_4 heterojunction photocatalyst to remove NOR was discussed.

2. Results and discussions

2.1. XRD Analysis

To examine the microstructure and ensure that the samples have no impurities, the XRD patterns of BSO, CN, and BSCN samples are exhibited in Figure 1. As for the CN pattern in Figure 1a, the aromatic interlayer stacking peak of the (002) crystal face appears pronouncedly at 2θ = 27.6°, in line with the CN standard PDF card (JCPDS No. 87-1526) [27]. The BSO pattern shows, in Figure 1b, several peaks located at 2θ = 14.3°, 23.4°, 28.8°, 33.4°, 43.8°, 47.9°, 54.0°, 56.9°, and 59.7°, corresponding to the (111), (220), (222), (400), (511), (440), (620), (622), and (444) crystal planes, and they are similar to the BSO standard PDF card (JCPDS No. 87-0284) [28]. Moreover, the average crystallite size of the BSO sample was 22.3 nm, as determined by the Scherrer equation. In the pattern of BSCN heterojunction photocatalysts (Figure 1c), the characteristic peaks of BSO and CN emerged simultaneously, and the peaks of the CN (002) plane moved to a higher angle, thus indicating that the heterojunction photocatalyst was successfully fabricated [29]. Moreover, all peaks are sharp, and there are no extra peaks in the pattern, thus demonstrating high crystallinity and no other miscellaneous products in the samples [30].

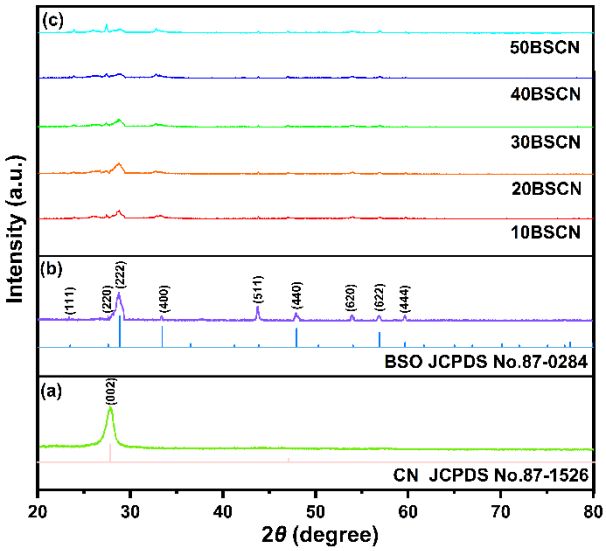

Figure 1. XRD patterns of CN (**a**), BSO (**b**), 10BSCN, 20BSCN, 30BSCN, 40BSCB, and 50BSCN (**c**).

2.2. FTIR Analysis

The bonding systems of BSO, CN, and BSCN were characterized by FTIR, and the results are provided in Figure 2. The characteristic absorption bands at 532 and 630 cm^{-1} belong to the Bi–O and Sn–O vibrations of BSO, respectively [31]. The triazine ring structure of CN causes the peak at 808 cm^{-1} [32]. In addition, the C–N and C=N bending vibration of CN induce the peaks at the range of 1200–1650 cm^{-1} [33]. The wide peak at the wavelength of 3000~3691 cm^{-1} can be attributed to the N–H functional group in the samples [34]. The spectra of BSCN heterojunction photocatalyst have similar absorption peaks of monomer BSO and CN, which are consistent with XRD results.

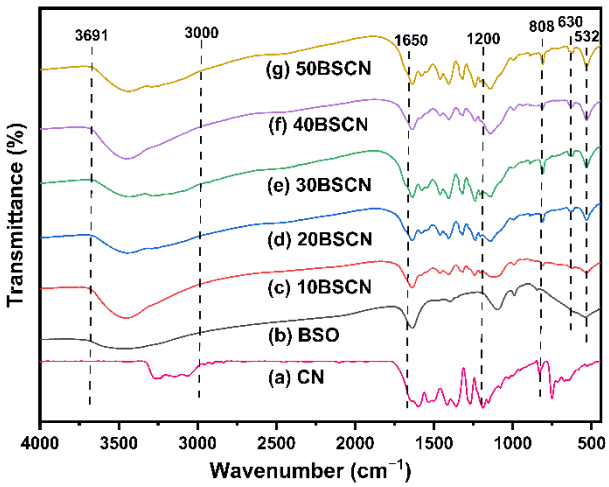

Figure 2. FTIR patterns of CN (**a**), BSO (**b**), 10BSCN (**c**), 20BSCN (**d**), 30BSCN (**e**), 40BSCN (**f**), and 50BSCN (**g**).

2.3. XPS Analysis

As shown in Figure 3, XPS was employed to examine the chemical state of the BSCN sample. The survey spectrum (Figure 3a) demonstrates the existence of bismuth, stannum, oxygen, carbon, and nitrogen in the BSCN sample. In Figure 3b, two peaks located at 159.4 eV and 164.7 eV belong to Bi $4f_{7/2}$ and Bi $4f_{5/2}$ in BSO and symbolize the chemical state of bismuth as +3 [35]. The peaks at 486.9 and 495.3 eV in Figure 3c correspond to the Sn $3d_{5/2}$ and Sn $3d_{3/2}$ of BSO, revealing that the chemical state of stannum is +4 [36]. In Figure 3d, the O 1s peaks lie at 530.7 and 532.8 eV, conforming to the O^{2-} of BSO and hydroxyl groups

in the surrounding environment [37]. Figure 3e displays the spectrum of C 1s, and the peaks at 284.9 eV and 288.9 eV were fitted to sp^2-hybridized carbon of CN and adventitious carbon on the surface of the samples. In Figure 3f, the N 1s spectrum exhibits three peaks at 398.8, 399.9, and 401.0 eV assigned at the triazine rings (C–N=C), tertiary nitrogen (N–(C_3)), and O–N bond, respectively [38].

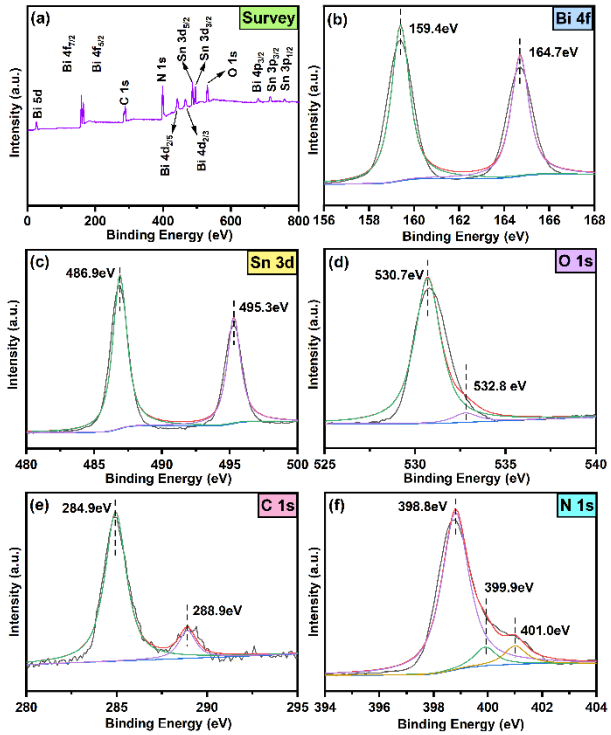

Figure 3. XPS survey pattern of BSCN (**a**); the high-resolution XPS spectra of Bi 4f (**b**), Sn 3d (**c**), O 1s (**d**), C 1s (**e**), and N 1s (**f**).

2.4. SEM and TEM Analysis

To observe the microscopic details and further investigate the photocatalytic performance of samples, the high-magnification SEM images of CN, BSO, and BSCN are disclosed in Figure 4. In Figure 4a, we can see that globular BSO particles are uniformly distributed with a particle size of 15–40 nm. Sheet-shape CNs stacked on top of each other can be clearly seen in Figure 4b. As shown in Figure 4c,d, the BSO particles are deposited on the CN sheet, thus confirming the formation of the BSCN heterojunction. Furthermore, the construction of BSCN heterojunction forms a relatively complex surface morphology, enriches the active points in the photocatalytic process, and contributes to the improvement of photocatalytic activity.

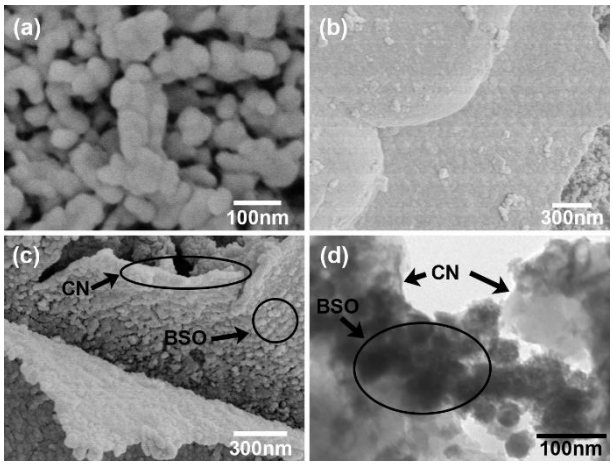

Figure 4. SEM patterns of BSO sample (**a**), CN sample (**b**), and BSCN sample (**c**); and TEM pattern of BSCN sample (**d**).

2.5. UV–Vis DRS Analysis

In order to figure out the optical absorption of the samples, the UV–Vis spectra of the BSO, CN, and BSCN composites are exhibited in Figure 5a, and the high-resolution images of the BSCN image are shown in Figure 5b. Obviously, the absorption edges of monomer BSO and CN were about 441 and 450 nm, whereas the absorption edges of 10BSCN, 20BSCN, 30BSCN, 40BSCN, and 50BSCN were 476, 482, 475, 471, and 475 nm, which experienced a dramatic redshift. Estimating by Tauc formula (in Figure 6), the band gap values (E_g) of BSO, CN, 10BSCN, 20BSCN, 30BSCN, 40BSCN, and 50BSCN were 2.81, 2.75, 2.60, 2.57, 2.61, 2.63, and 2.61 eV, respectively [39]. Assuredly, these samples have a strong responsiveness under the visible-light region, and the establishment of BSCN heterojunction structure enhanced the light-absorption properties.

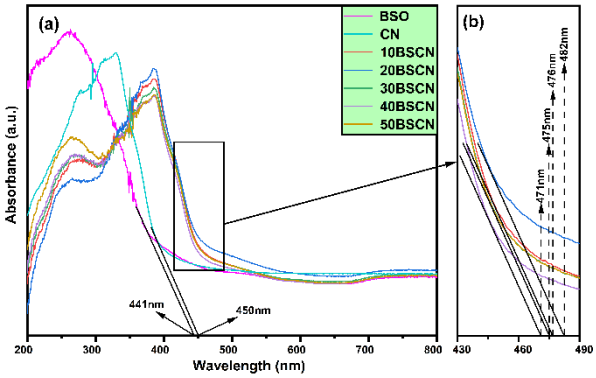

Figure 5. The UV–Vis diffuse reflection patterns (**a**) and the high-resolution pattern (**b**).

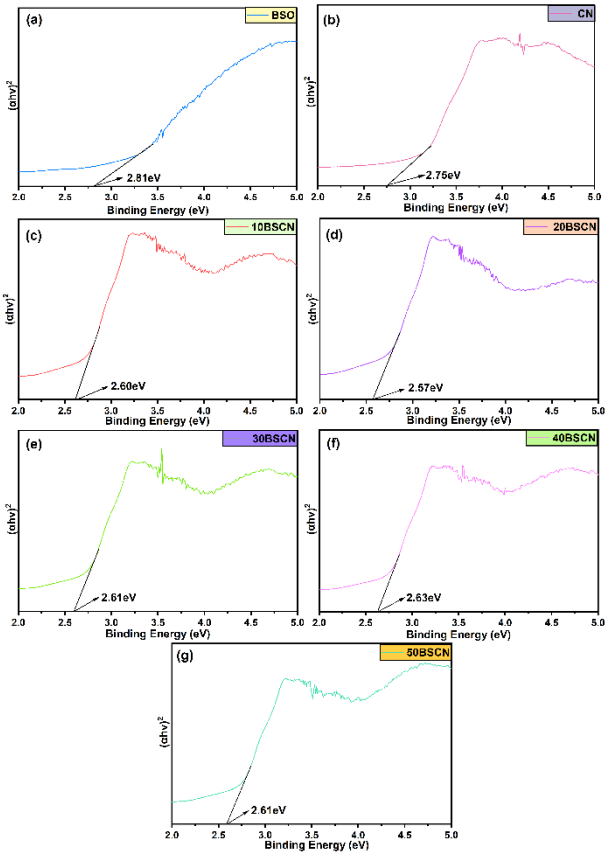

Figure 6. DRS analysis of BSO (**a**), CN (**b**), 10BSCN (**c**), 20BSCN (**d**), 30BSCN (**e**), 40BSCN (**f**), and 50BSCN (**g**).

2.6. PL Analysis

Typically, the rapid recombination of photogenerated electron and holes will hinder the photocatalytic process. Figure 7 presents the recombination efficiency of photogenerated electrons and holes of BSCN heterojunction photocatalysts with an excited wavelength at 290 nm. The higher the peak intensity of PL, the higher the recombination efficiency of photogenerated electrons and holes [40]. Clearly, with the increase of the amount of BSO, the peak of BSCN heterojunction photocatalysts becomes weaker than that of pristine CN. The 20BSCN sample possessed the weakest peak, which confirmed that the formation of heterojunction alleviates the recombination of photogenerated electron–hole pairs.

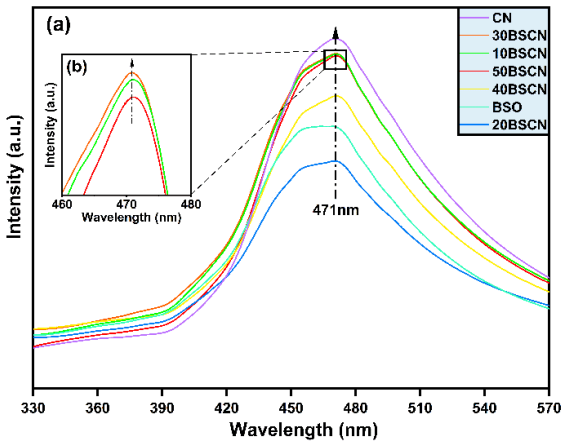

Figure 7. PL emission patterns of BSO, CN and BSCN (**a**) and the high-definition pattern (**b**).

2.7. Photocatalytic Performance

The photodegradation efficiency of NOR by the BSCN heterojunction in visible light is shown in Figure 8. In Figure 8a and Table 1, there is no NOR decomposed without the addition of a photocatalyst. The CN and BSO can remove 31% and 40% of NOR in the solution within 3 h. However, after the addition of BSCN composite photocatalysts, the visible light degradation rate of NOR has a dramatic increase. The 20BSCN sample eliminated 94% of NOR within 3 h, which was 3.03 times that of BSO and 2.35 times that of CN. And 10BSCN, 30BSCN,40BSCN and 50BSCN removed 78%, 70%, 87% and 85% of NOR, respectively. Figure 8b exhibited the kinetic curves of NOR degradation of the samples. The kinetic constants of BSO, CN, 10BSCN, 20BSCN, 30BSCN, 40BSCN and 50BSCN were 0.00325, 0.00216, 0.00703, 0.01261, 0.0068 0.00997 and 0.00932 min^{-1}, respectively. The reaction rate of 20BSCN is 3.88 times higher than BSO and 5.83 times higher than CN. Evidently, with the increase of BSO, the degradation activity of NOR by BSCN gradually increased and reached the maximum at 20BSCN, then decreased. 20BSCN has eminent photocatalytic performance of NOR degradation under the visible light irradiation. In addition, the degree of NOR mineralization before and after the degradation of 20BSCN was investigated by Total Organic Carbon (TOC) test. In the initial solution, the TOC concentration is 20.61 mg/L. Whereas the concentration decreased to 3.55 mg/L after the photocatalytic process, indicating the 20BSCN sample effectively mineralized the NOR pollutant in the solution. Furthermore, a comparison of photocatalytic performance between BSCN and the other g-C_3N_4-based heterojunctions are displayed in Table 2.

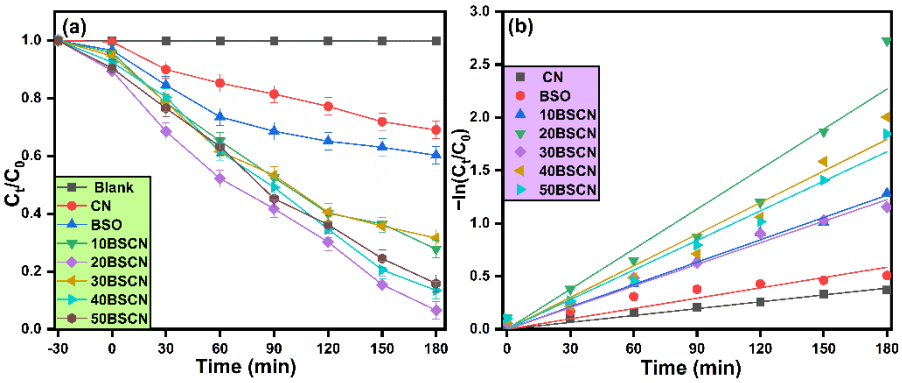

Figure 8. Photocatalytic degradation performance of NOR by BSO, CN, and BSCN heterojunction photocatalysts under visible light (**a**); kinetic curves of NOR degradation (**b**).

Table 1. Photocatalytic performance of as-prepared samples.

Sample Name	Degradation (%)	K (min^{-1})	R^2
BSO	40%	0.00325	0.95248
CN	31%	0.00216	0.9814
10BSCN	78%	0.00703	0.98684
20BSCN	94%	0.01261	0.96041
30BSCN	70%	0.0068	0.98331
40BSCN	87%	0.00997	0.97395
50BSCN	85%	0.00932	0.98105

Table 2. Comparison of photocatalytic performance with other g-C_3N_4 based heterojunction photocatalyst.

Sample Name	Degradation	Time	Light Source	Target	Reference
CeO_2/g-C_3N_4	88.6%	60 min	Visible light	Norfloxacin	[41]
$NiWO_4$/g-C_3N_4	97%	60 min	Visible light	Norfloxacin	[42]
$LaNiO_3$/g-C_3N_4	96%	300 min	Visible light	Tetracycline	[43]
TiO_2/g-C_3N_4	99.4%	120 min	Visible light	Tetracycline	[44]
$ZnIn_2S_4$/g-C_3N_4	98%	300 min	Visible light	Metronidazole	[45]
BiOCl/g-C_3N_4	95%	180 min	Visible light	Metronidazole	[46]
$Bi_2Sn_2O_7$/g-C_3N_4	94%	180 min	Visible light	Norfloxacin	This work

The reusable photocatalyst is an important parameter affecting the practical application of photocatalysts. As shown in Figure 9, the degradation efficiency of NOR showed an inconspicuous decrease after each cycle. The loss of the 20BSCN photocatalyst in the process of centrifuging separation, washing, and drying induced this phenomenon, whereas the 20BSCN sample still decomposed 89% of NOR after five continuous degradation processes, thus confirming the great stability of it.

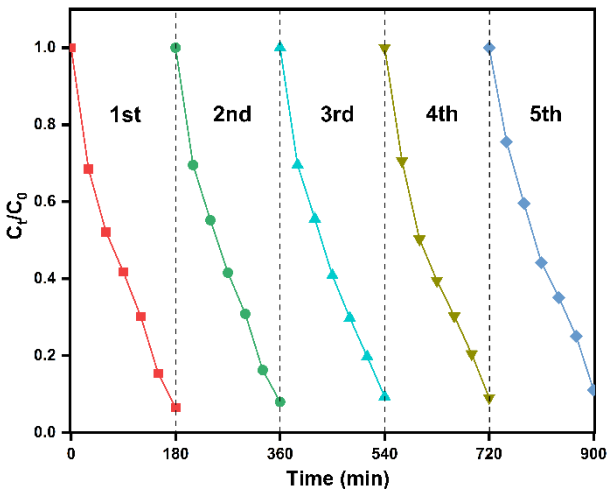

Figure 9. Reusability of photocatalytic activities experiment on 20BSCN photocatalysts.

2.8. Possible Mechanism

Figure 10a illustrates the possible mechanism by which BSCN improves the photocatalytic performance of NOR degradation. The valence band (VB) and conduction band (CB) potentials of BSO and CN are estimated by the following equation [47]:

$$E_{VB} = X - E^e + 0.5E_g, \quad (1)$$

$$E_{CB} = E_{VB} - E_g, \quad (2)$$

In these equations, E_{VB} and E_{CB} represent the CB and VB potential of photocatalysts, and X is the electronegativity of the photocatalysts. For BSO and CN, the value of X is 6.08 eV [22] and 4.72 eV [48]. The value of E^e is about 4.5 eV, which represents the energy of free electrons on the hydrogen scale [49]. Hence, the CB_{BSO} and CB_{CN} were estimated at 0.18 eV and −1.23 eV. The VB_{BSO} and VB_{CN} were calculated at 2.99 eV and 1.52 eV, respectively. With these values identified, the transfer path of photogenerated electrons can be inferred as the Z-scheme.

Primarily, both BSO and CN respond to visible light due to their narrow bandgap. Thus, the photogenerated electrons jump from their VB to their CB under the excitation of visible light [50]. Typically, the rapid recombination of photocarriers is one of the vital factors hindering photocatalytic activity. After the heterojunction is formed, the electron transfer path changes dramatically. The adjacent position of CB_{BSO} and VB_{CN} makes the electrons generated by photoexcitation on CB_{BSO} recombine with the holes on VB_{CN} [51], as there are not enough photogenerated holes in VB_{CN} to recombine with photogenerated electrons in CB_{CN}. Meanwhile, the electrons on CB_{BSO} transfer to VB_{CN}, and no photogenerated electrons return to VB_{BSO} to recombine with the photoinduced holes, thus greatly reducing the recombination efficiency of photogenerated carriers and improving the photocatalytic activity, in accordance with the PL result [52]. In addition, the position of CB_{CN} is more negative than the potential $O_2/\cdot O_2^-$ (−0.33 eV) [53]. The photoinduced electron concentrate on the CB_{CN} will convert the O_2 in the solution to active substance $\cdot O_2^-$ [54]. The VB_{CN} was more negative than the reduction potential for $\cdot OH/OH^-$ (+1.99 eV) and $H_2O/\cdot OH$ (+2.27 eV) [55]. In other words, even if photogenerated holes are concentrated on VB_{CN}, it cannot react with water in the solution to produce active substance ·OH [56]. Whereas VB_{BSO} was more positive than the reduction potential for $\cdot OH/OH^-$, the photoinduced holes on VB_{BSO} will produce the active substance, ·OH. In Figure 10b, a radicals' quenching experiment was performed to investigate the active substances in photocatalytic processes. The silver nitrate ($AgNO_3$), anhydrous ethanol (C_2H_6O), benzoquinone (BQ), and ethylene glycol (IPA) were adopted as the electron (e^-) quencher, hole (h^+) quencher, hydroxyl radical (·OH) quencher, and superoxide radical ($\cdot O_2^-$) quencher, respectively. After the addition of quenchers, the degradation activity of BSCN to NOR was significantly reduced, indicating that these active substances played an important role in the degradation process. Finally, the active substance converts the NOR contaminant in the solution into CO_2, H_2O and other harmless substances [57]. To sum up, the construction of the BSCN heterojunction prolongs the life of photocarriers and improves the photocatalytic activity to degrade NOR.

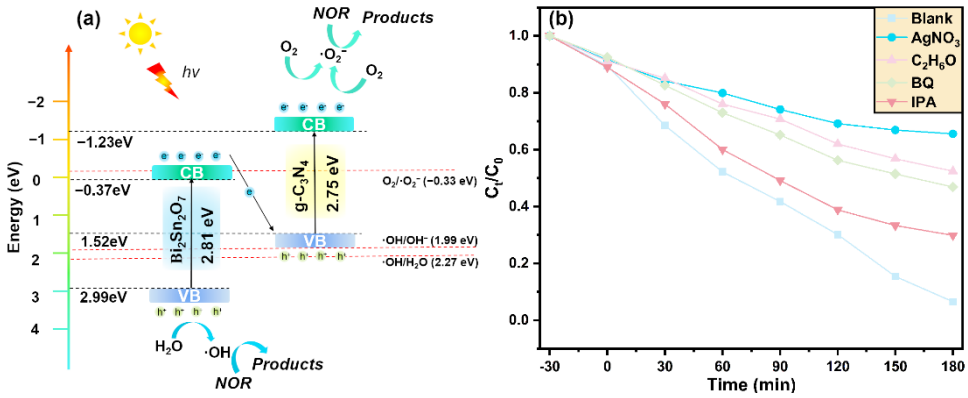

Figure 10. Possible mechanism of BSCN composite photocatalyst (**a**) and results of radicals quenching experiments (**b**).

3. Materials and Methods

3.1. Materials

All reagents used in this work were supplied as AR-grade chemicals from Sinopharm Chemical Reagent Co (Shanghai, China), without further purification.

3.2. Preparation of g-C_3N_4 Photocatalyst

Following the directions of previous reports [58], 10 g of melamine was added into a covered ceramic crucible and sintered at 550 °C in a muffle furnace for 4 h. After cooling and triturating, the primrose yellow powder was CN.

3.3. Synthesis of $Bi_2Sn_2O_7$ Photocatalyst

BSO photocatalyst was synthesis by a facile hydrothermal process according to the antecedent studies [59]. Initially, $Bi(NO_3)_3{\cdot}5H_2O$ (9 mmol) and $K_2SnO_3{\cdot}3H_2O$ (9 mmol) were dissolved in 40 mL deionized water, respectively. The above solutions were blended, and the pH value was adjusted to 12 by adding $NH_3{\cdot}H_2O$. After 30 min of vigorous continuous stirring, the obtained hybrid was sealed in a 100 mL stainless autoclave lined with polytetrafluoroethylene in a vacuum-drying oven at 180 °C for 16 h. After cooling to room temperature, the milky white precipitate was filtered and washed with distilled water and absolute ethanol several times, respectively. Finally, the precursor was dried in a vacuum drying oven at 80 °C overnight.

3.4. Fabrication of $Bi_2Sn_2O_7$/g-C_3N_4 Heterojunction Photocatalysts

BSCN heterojunction were fabricated by a facile ultrasound-assisted hydrothermal approach [60]. Typically, appropriate amounts of BSO and CN powder were scattered in 40 mL of ethanol and subjected to ultrasonic vibration for 30 min. The resulting mixture was poured into a 100 mL stainless autoclave lined with polytetrafluoroethylene and placed in vacuum-drying oven at 180 °C for 24 h. The sediment at the bottom was cleaned with DI water and ethanol several times after cooling to room temperature, and then it was dried in a vacuum-drying oven overnight. The dried product was BSCN heterojunction photocatalyst, and the different loading BSOs of the BSCN samples were obtained in the same way.

3.5. Characterization

The X-ray diffractometer (XRD) pattern was manifested by Shimadzu XRD-6000 (Kyoto, Japan). The FTIR spectrum was analyzed via a Bruker AXS TENSOR 27 FTIR spectrometer (Karlsruhe, Germany). Hitachi SU8010 scanning microscopy (Tokyo, Japan) and JEOL JEM-2100 transmission electron microscopy (Tokyo, Japan) were employed to observe the surface morphology of samples. The XPS pattern of samples was derived from an ESCALAB250 analysis system by Thermo VG (Waltham, MA, USA). The PerkinElmer Lambda 35 Spectrophotometer (Waltham, MA, USA) was adopted to measure the UV–Vis spectra of samples. The Shimadzu RF-540 Fluorescence Spectrophotometer (Kyoto, Japan) was used to record the PL spectra.

3.6. Photocatalytic Activity and Stability Evaluation

To evaluate the performance of the as-prepared samples, 0.02 g CN, BSO, 10BSCN, 20BSCN, 30BSCN, 40BSCN, and 50BSCN photocatalyst samples were placed in 100 mL 20 mg/L NOR solution and stirred continuously for 30 min, away from light, to achieve an adsorption–desorption equilibrium, respectively. The visible light source was simulated by a 500 W xenon lamp with a UV cutoff filter. After the lamp was turned on, the solutions were sampled and filtered per 30 min to acquire the absorbance, using UV–Vis spectroscopy, and calculate the degradation rate. The concentration of NOR was estimated according to the initial NOR absorption value (C_0) and residual NOR absorption value (C_t). All the steps were performed at room temperature.

The recycling experiment was designed to understand the stability of BSCN heterojunction photocatalyst. After each process of NOR degradation, the photocatalyst sample in the solution was separated by centrifugation and then washed by DI water and ethanol. After being dried in a vacuum oven overnight, the recollected photocatalyst was used in the next cycle experiment and repeated five times.

4. Conclusions

In this work, a $Bi_2Sn_2O_7$/g-C_3N_4 heterojunction photocatalyst was synthesized with an ultrasound-assisted hydrothermal method and characterized by XRD, FTIR, XPS, SEM, TEM, UV–Vis DRS, and PL. With 20% $Bi_2Sn_2O_7$ loaded, the heterojunction photocatalyst

can remove 94% NOR within 3 h, under visible light, which was 2.35 times as much as g-C_3N_4 and 3.03 times as much as $Bi_2Sn_2O_7$. We deduced that improving the separation efficiency of photogenerated electron holes induced the enhanced photocatalytic performance in NOR degradation. Moreover, 89% NOR was eliminated after five times of recycling degradation, indicating a distinguished stability and cyclability of the heterojunction photocatalyst. In brief, the $Bi_2Sn_2O_7$/g-C_3N_4 heterojunction photocatalyst is a promising and ideal photocatalyst for the treatment of antibiotic pollution in water.

Author Contributions: Supervision, H.L.; methodology, S.H.; writing—original draft preparation, H.X.; writing—review and editing, Z.Z. All authors have read and agreed to the published version of the manuscript.

Funding: This research was funded by "Research and Development Fund of Dalian Naval Academy, grant number No.2021-027".

Institutional Review Board Statement: Not applicable.

Informed Consent Statement: Not applicable.

Data Availability Statement: Not applicable.

Conflicts of Interest: The authors declare no conflict of interest.

References

1. Wang, K.; Li, Y.; Zhang, G.; Li, J.; Wu, X. 0D Bi Nanodots/2D Bi_3NbO_7 Nanosheets Heterojunctions for Efficient Visible Light Photocatalytic Degradation of Antibiotics: Enhanced Molecular Oxygen Activation and Mechanism Insight. *Appl. Catal. B Environ.* **2019**, *240*, 39–49. https://doi.org/10.1016/j.apcatb.2018.08.063.
2. Jiang, Y.; Zhang, M.; Xin, Y.; Chai, C.; Chen, Q. Construction of Immobilized CuS/TiO_2 Nanobelts Heterojunction Photocatalyst for Photocatalytic Degradation of Enrofloxacin: Synthesis, Characterization, Influencing Factors and Mechanism Insight. *J. Chem. Technol. Biotechnol.* **2019**, *94*, 2219–2228. https://doi.org/10.1002/jctb.6006.
3. Xu, M.; Wang, Y.; Ha, E.; Zhang, H.; Li, C. Reduced Graphene Oxide/$Bi_4O_5Br_2$ Nanocomposite with Synergetic Effects on Improving Adsorption and Photocatalytic Activity for the Degradation of Antibiotics. *Chemosphere* **2021**, *265*, 129013. https://doi.org/10.1016/j.chemosphere.2020.129013.
4. Kumar, R.; Barakat, M.A.; Al-Mur, B.A.; Alseroury, F.A.; Eniola, J.O. Photocatalytic Degradation of Cefoxitin Sodium Antibiotic Using Novel BN/$CdAl_2O_4$ Composite. *J. Clean. Prod.* **2020**, *246*, 119076. https://doi.org/10.1016/j.jclepro.2019.119076.
5. Kamranifar, M.; Allahresani, A.; Naghizadeh, A. Synthesis and Characterizations of a Novel $CoFe_2O_4$@CuS Magnetic Nanocomposite and Investigation of Its Efficiency for Photocatalytic Degradation of Penicillin G Antibiotic in Simulated Wastewater. *J. Hazard. Mater.* **2019**, *366*, 545–555. https://doi.org/10.1016/j.jhazmat.2018.12.046.
6. Li, J.; Fang, W.; Yu, C.; Zhou, W.; Zhu, L.; Xie, Y. Ag-Based Semiconductor Photocatalysts in Environmental Purification. *Appl. Surf. Sci.* **2015**, *358*, 46–56.
7. Hunge, Y.M.; Yadav, A.A.; Khan, S.; Takagi, K.; Suzuki, N.; Teshima, K.; Terashima, C.; Fujishima, A. Photocatalytic Degradation of Bisphenol A Using Titanium Dioxide@nanodiamond Composites under UV Light Illumination. *J. Colloid Interface Sci.* **2021**, *582*, 1058–1066. https://doi.org/10.1016/j.jcis.2020.08.102.
8. Wang, J.; Zhang, G.; Li, J.; Wang, K. Novel Three-Dimensional Flowerlike BiOBr/Bi_2SiO_5 p-n Heterostructured Nanocomposite for Degradation of Tetracycline: Enhanced Visible Light Photocatalytic Activity and Mechanism. *ACS Sustain. Chem. Eng.* **2018**, *6*, 14221–14229. https://doi.org/10.1021/acssuschemeng.8b02869.
9. Zhou, J.; Zhang, Z.; Kong, X.; He, F.; Zhao, R.; Wu, R.; Wei, T.; Wang, L.; Feng, J. A Novel P-N Heterojunction with Staggered Energy Level Based on $ZnFe_2O_4$ Decorating SnS_2 Nanosheet for Efficient Photocatalytic Degradation. *Appl. Surf. Sci.* **2020**, *510*, 145442. https://doi.org/10.1016/j.apsusc.2020.145442.
10. Wan, H.; Yao, W.; Zhu, W.; Tang, Y.; Ge, H.; Shi, X.; Duan, T. Fe-N Co-Doped SiO_2 @TiO_2 Yolk-Shell Hollow Nanospheres with Enhanced Visible Light Photocatalytic Degradation. *Appl. Surf. Sci.* **2018**, *444*, 355–363. https://doi.org/10.1016/j.apsusc.2018.03.016.
11. Santos, L.M.M.; Nascimento, M.M.; Borges, S. dos S.; Bomfim, E.; Macedo, V. de J.; Silva, L.A. Green Photocatalytic Remediation of Fenthion Using Composites with Natural Red Clay and Non-Toxic Metal Oxides with Visible Light Irradiation. *Environ. Technol.* **2021**, *Online ahead of print*. https://doi.org/10.1080/09593330.2021.1964611.
12. Jalalah, M.; Faisal, M.; Bouzid, H.; Park, J.G.; Al-Sayari, S.A.; Ismail, A.A. Comparative Study on Photocatalytic Performances of Crystalline α- and β-Bi_2O_3 Nanoparticles under Visible Light. *J. Ind. Eng. Chem.* **2015**, *30*, 183–189. https://doi.org/10.1016/j.jiec.2015.05.020.
13. Liang, Q.; Jin, J.; Liu, C.; Xu, S.; Li, Z. Constructing a Novel P-n Heterojunction Photocatalyst $LaFeO_3$/g-C_3N_4 with Enhanced Visible-Light-Driven Photocatalytic Activity. *J. Alloys Compd.* **2017**, *709*, 542–548. https://doi.org/10.1016/j.jallcom.2017.03.190.

14. Huang, Y.; Kang, S.; Yang, Y.; Qin, H.; Ni, Z.; Yang, S.; Li, X. Facile Synthesis of Bi/Bi_2WO_6 Nanocomposite with Enhanced Photocatalytic Activity under Visible Light. *Appl. Catal. B Environ.* **2016**, *196*, 89–99. https://doi.org/10.1016/j.apcatb.2016.05.022.
15. Zhao, W.; Feng, Y.; Huang, H.; Zhou, P.; Li, J.; Zhang, L.; Dai, B.; Xu, J.; Zhu, F.; Sheng, N.; et al. A Novel Z-Scheme Ag_3VO_4/$BiVO_4$ Heterojunction Photocatalyst: Study on the Excellent Photocatalytic Performance and Photocatalytic Mechanism. *Appl. Catal. B Environ.* **2019**, *245*, 448–458. https://doi.org/10.1016/j.apcatb.2019.01.001.
16. Song, T.; Yu, X.; Tian, N.; Huang, H. wei Preparation, Structure and Application of g-C_3N_4/BiOX Composite Photocatalyst. *Int. J. Hydrog. Energy* **2021**, *46*, 1857–1878.
17. Han, C.; Su, P.; Tan, B.; Ma, X.; Lv, H.; Huang, C.; Wang, P.; Tong, Z.; Li, G.; Huang, Y.; et al. Defective Ultra-Thin Two-Dimensional g-C_3N_4 Photocatalyst for Enhanced Photocatalytic H_2 Evolution Activity. *J. Colloid Interface Sci.* **2021**, *581*, 159–166. https://doi.org/10.1016/j.jcis.2020.07.119.
18. Feng, D.; Cheng, Y.; He, J.; Zheng, L.; Shao, D.; Wang, W.; Wang, W.; Lu, F.; Dong, H.; Liu, H.; et al. Enhanced Photocatalytic Activities of g-C_3N_4 with Large Specific Surface Area via a Facile One-Step Synthesis Process. *Carbon N. Y.* **2017**, *125*, 454–463. https://doi.org/10.1016/j.carbon.2017.09.084.
19. Sun, Y.; Qi, X.; Li, R.; Xie, Y.; Tang, Q.; Ren, B. Hydrothermal Synthesis of 2D/2D BiOCl/g-C_3N_4 Z-Scheme: For TC Degradation and Antimicrobial Activity Evaluation. *Opt. Mater.* **2020**, *108*, 110170. https://doi.org/10.1016/j.optmat.2020.110170.
20. Hu, K.; Li, R.; Ye, C.; Wang, A.; Wei, W.; Hu, D.; Qiu, R.; Yan, K. Facile Synthesis of Z-Scheme Composite of TiO_2 Nanorod/g-C_3N_4 Nanosheet Efficient for Photocatalytic Degradation of Ciprofloxacin. *J. Clean. Prod.* **2020**, *253*, 120055. https://doi.org/10.1016/j.jclepro.2020.120055.
21. Zhang, D.; Qi, J.; Ji, H.; Li, S.; Chen, L.; Huang, T.; Xu, C.; Chen, X.; Liu, W. Photocatalytic Degradation of Ofloxacin by Perovskite-Type $NaNbO_3$ Nanorods Modified g-C_3N_4 Heterojunction under Simulated Solar Light: Theoretical Calculation, Ofloxacin Degradation Pathways and Toxicity Evolution. *Chem. Eng. J.* **2020**, *400*, 125918. https://doi.org/10.1016/j.cej.2020.125918.
22. Xu, W.; Fang, J.; Chen, Y.; Lu, S.; Zhou, G.; Zhu, X.; Fang, Z. Novel Heterostructured Bi_2S_3/$Bi_2Sn_2O_7$ with Highly Visible Light Photocatalytic Activity for the Removal of Rhodamine B. *Mater. Chem. Phys.* **2015**, *154*, 30–37. https://doi.org/10.1016/j.matchemphys.2015.01.040.
23. Zhang, D.; Yang, Z.; Hao, J.; Zhang, T.; Sun, Q.; Wang, Y. Boosted Charge Transfer in Dual Z-Scheme $BiVO_4$@$ZnIn_2S_4$/$Bi_2Sn_2O_7$ Heterojunctions: Towards Superior Photocatalytic Properties for Organic Pollutant Degradation. *Chemosphere* **2021**, *276*, 130226. https://doi.org/10.1016/j.chemosphere.2021.130226.
24. Elhaddad, E.; Rehman, W.; Waseem, M.; Nawaz, M.; Haq, S.; Guo, C.Y. Fabrication of Highly Efficient $Bi_2Sn_2O_7$/C_3N_4 Composite with Enhanced Photocatalytic Activity for Degradation of Organic Pollutants. *J. Inorg. Organomet. Polym. Mater.* **2021**, *31*, 172–179. https://doi.org/10.1007/s10904-020-01726-z.
25. Zhao, X.; Yu, J.; Cui, H.; Wang, T. Preparation of Direct Z-Scheme $Bi_2Sn_2O_7$/g-C_3N_4 Composite with Enhanced Photocatalytic Performance. *J. Photochem. Photobiol. A Chem.* **2017**, *335*, 130–139. https://doi.org/10.1016/j.jphotochem.2016.11.011.
26. Heidari, S.; Haghighi, M.; Shabani, M. Ultrasound Assisted Dispersion of $Bi_2Sn_2O_7$-C_3N_4 Nanophotocatalyst over Various Amount of Zeolite Y for Enhanced Solar-Light Photocatalytic Degradation of Tetracycline in Aqueous Solution. *Ultrason. Sonochemistry* **2018**, *43*, 61–72. https://doi.org/10.1016/j.ultsonch.2018.01.001.
27. Hu, T.; Dai, K.; Zhang, J.; Zhu, G.; Liang, C. One-Pot Synthesis of Step-Scheme Bi_2S_3/Porous g-C_3N_4 Heterostructure for Enhanced Photocatalytic Performance. *Mater. Lett.* **2019**, *257*, 126740. https://doi.org/10.1016/j.matlet.2019.126740.
28. Wu, J.; Huang, F.; Lü, X.; Chen, P.; Wan, D.; Xu, F. Improved Visible-Light Photocatalysis of Nano-$Bi_2Sn_2O_7$ with Dispersed s-Bands. *J. Mater. Chem.* **2011**, *21*, 3872–3876. https://doi.org/10.1039/c0jm03252b.
29. Miao, X.; Shen, X.; Wu, J.; Ji, Z.; Wang, J.; Kong, L.; Liu, M.; Song, C. Fabrication of an All Solid Z-Scheme Photocatalyst g-C_3N_4/GO/AgBr with Enhanced Visible Light Photocatalytic Activity. *Appl. Catal. A Gen.* **2017**, *539*, 104–113. https://doi.org/10.1016/j.apcata.2017.04.009.
30. Mohamed, R.M.; Ismail, A.A. Mesoporous $BiVO_4$/2D-g-C_3N_4 Heterostructures for Superior Visible Light-Driven Photocatalytic Reduction of Hg(II) Ions. *Ceram. Int.* **2021**, *47*, 26063–26073. https://doi.org/10.1016/j.ceramint.2021.06.012.
31. Gnanamoorthy, G.; Muthamizh, S.; Sureshbabu, K.; Munusamy, S.; Padmanaban, A.; Kaaviya, A.; Nagarajan, R.; Stephen, A.; Narayanan, V. Photocatalytic Properties of Amine Functionalized $Bi_2Sn_2O_7$/rGO Nanocomposites. *J. Phys. Chem. Solids* **2018**, *118*, 21–31. https://doi.org/10.1016/j.jpcs.2018.02.042.
32. Liu, L.; Qi, Y.; Hu, J.; An, W.; Lin, S.; Liang, Y.; Cui, W. Stable Cu_2O@g-C_3N_4 Core@shell Nanostructures: Efficient Visible-Light Photocatalytic Hydrogen Evolution. *Mater. Lett.* **2015**, *158*, 278–281. https://doi.org/10.1016/j.matlet.2015.06.034.
33. Wang, M.; Zeng, Y.; Dong, G.; Wang, C. Br-Doping of g-C_3N_4 towards Enhanced Photocatalytic Performance in Cr(VI) Reduction. *Chin. J. Catal.* **2020**, *41*, 1498–1510.
34. Shi, L.; Wang, F.; Sun, J. The Preparation of Spherical Mesoporous g-C_3N_4 with Highly Improved Photocatalytic Performance for H_2 Production and Rhodamine B Degradation. *Mater. Res. Bull.* **2019**, *113*, 115–121. https://doi.org/10.1016/j.materresbull.2019.01.028.
35. Xing, Y.; Que, W.; Yin, X.; He, Z.; Liu, X.; Yang, Y.; Shao, J.; Kong, L.B. In_2O_3/$Bi_2Sn_2O_7$ Heterostructured Nanoparticles with Enhanced Photocatalytic Activity. *Appl. Surf. Sci.* **2016**, *387*, 36–44. https://doi.org/10.1016/j.apsusc.2016.06.057.
36. Hu, C.; Zhuang, J.; Zhong, L.; Zhong, Y.; Wang, D.; Zhou, H. Significantly Enhanced Photocatalytic Activity of Visible Light Responsive AgBr/$Bi_2Sn_2O_7$ Heterostructured Composites. *Appl. Surf. Sci.* **2017**, *426*, 1173–1181. https://doi.org/10.1016/j.apsusc.2017.07.167.

37. Deng, Y.; Tang, L.; Zeng, G.; Wang, J.; Zhou, Y.; Wang, J.; Tang, J.; Liu, Y.; Peng, B.; Chen, F. Facile Fabrication of a Direct Z-Scheme Ag_2CrO_4/g-C_3N_4 Photocatalyst with Enhanced Visible Light Photocatalytic Activity. *J. Mol. Catal. A Chem.* **2016**, *421*, 209–221. https://doi.org/10.1016/j.molcata.2016.05.024.
38. Jiang, Y.; Liu, Q.; Tan, K.M.; Wang, F.; Ng, H.Y. Insights into Mechanisms, Kinetics and Pathway of Continuous Visible-Light Photodegradation of PPCPs via Porous g-C_3N_4 with Highly Dispersed Fe(III) Active Sites. *Chem. Eng. J.* **2021**, *423*, 130095. https://doi.org/10.1016/j.cej.2021.130095.
39. Ragupathi, V.; Raja, M.A.; Panigrahi, P.; Ganapathi Subramaniam, N. CuO/g-C_3N_4 Nanocomposite as Promising Photocatalyst for Photoelectrochemical Water Splitting. *Optik* **2020**, *208*, 164569. https://doi.org/10.1016/j.ijleo.2020.164569.
40. Zhao, S.; Chen, S.; Yu, H.; Quan, X. g-C_3N_4/TiO_2 Hybrid Photocatalyst with Wide Absorption Wavelength Range and Effective Photogenerated Charge Separation. *Sep. Purif. Technol.* **2012**, *99*, 50–54. https://doi.org/10.1016/j.seppur.2012.08.024.
41. Liu, W.; Zhou, J.; Yao, J. Shuttle-like CeO_2/g-C_3N_4 Composite Combined with Persulfate for the Enhanced Photocatalytic Degradation of Norfloxacin under Visible Light. *Ecotoxicol. Environ. Saf.* **2020**, *190*, 110062. https://doi.org/10.1016/j.ecoenv.2019.110062.
42. Lakshmi Prabavathi, S.; Muthuraj, V. Superior Visible Light Driven Photocatalytic Degradation of Fluoroquinolone Drug Norfloxacin over Novel $NiWO_4$ Nanorods Anchored on g-C_3N_4 Nanosheets. *Colloids Surf. A Physicochem. Eng. Asp.* **2019**, *567*, 43–54.
43. Zhou, X.; Chen, Y.; Li, C.; Zhang, L.; Zhang, X.; Ning, X.; Zhan, L.; Luo, J. Construction of $LaNiO_3$ Nanoparticles Modified g-C_3N_4 Nanosheets for Enhancing Visible Light Photocatalytic Activity towards Tetracycline Degradation. *Sep. Purif. Technol.* **2019**, *211*, 179–188. https://doi.org/10.1016/j.seppur.2018.09.075.
44. Zhang, B.; He, X.; Ma, X.; Chen, Q.; Liu, G.; Zhou, Y.; Ma, D.; Cui, C.; Ma, J.; Xin, Y. In Situ Synthesis of Ultrafine TiO_2 Nanoparticles Modified g-C_3N_4 Heterojunction Photocatalyst with Enhanced Photocatalytic Activity. *Sep. Purif. Technol.* **2020**, *247*, 116932. https://doi.org/10.1016/j.seppur.2020.116932.
45. Xu, Y.; Yifeng, E.; Wang, G. Controlled Growth of "Cookie-like" $ZnIn_2S_4$ Nanoparticles on g-C_3N_4 for Enhanced Visible Light Photocatalytic Activity. *Inorg. Chem. Commun.* **2019**, *108*, 107485. https://doi.org/10.1016/j.inoche.2019.107485.
46. Xu, Y.; Li, Z.; Fang, F.; Yifeng, E.; Zhao, G. Novel Visible-Light-Induced BiOCl/g-C_3N_4 Photocatalyst for Efficient Degradation of Metronidazole. *Inorg. Chem. Commun.* **2021**, *132*, 108820. https://doi.org/10.1016/j.inoche.2021.108820.
47. Gao, Y.; Lin, J.; Zhang, Q.; Yu, H.; Ding, F.; Xu, B.; Sun, Y.; Xu, Z. Facile Synthesis of Heterostructured YVO_4/g-C_3N_4/Ag Photocatalysts with Enhanced Visible-Light Photocatalytic Performance. *Appl. Catal. B Environ.* **2018**, *224*, 586–593. https://doi.org/10.1016/j.apcatb.2017.11.003.
48. Pan, T.; Chen, D.; Fang, J.; Wu, K.; Feng, W.; Zhu, X.; Fang, Z. Facile Synthesis of Iron and Cerium Co-Doped g-C_3N_4 with Synergistic Effect to Enhance Visible-Light Photocatalytic Performance. *Mater. Res. Bull.* **2020**, *125*, 110812. https://doi.org/10.1016/j.materresbull.2020.110812.
49. Zhang, B.; Hu, X.; Liu, E.; Fan, J. Novel S-Scheme 2D/2D BiOBr/g-C_3N_4 Heterojunctions with Enhanced Photocatalytic Activity. *Chin. J. Catal.* **2021**, *42*, 1519–1529. https://doi.org/10.1016/S1872-2067(20)63765-2.
50. Wang, T.; Quan, W.; Jiang, D.; Chen, L.; Li, D.; Meng, S.; Chen, M. Synthesis of Redox-Mediator-Free Direct Z-Scheme AgI/WO_3 Nanocomposite Photocatalysts for the Degradation of Tetracycline with Enhanced Photocatalytic Activity. *Chem. Eng. J.* **2016**, *300*, 280–290. https://doi.org/10.1016/j.cej.2016.04.128.
51. Jiang, E.; Song, N.; Che, G.; Liu, C.; Dong, H.; Yang, L. Construction of a Z-Scheme MoS_2/$CaTiO_3$ Heterostructure by the Morphology-Controlled Strategy towards Enhancing Photocatalytic Activity. *Chem. Eng. J.* **2020**, *399*, 125721. https://doi.org/10.1016/j.cej.2020.125721.
52. Luo, J.; Ning, X.; Zhan, L.; Zhou, X. Facile Construction of a Fascinating Z-Scheme AgI/$Zn_3V_2O_8$ Photocatalyst for the Photocatalytic Degradation of Tetracycline under Visible Light Irradiation. *Sep. Purif. Technol.* **2021**, *255*, 117691. https://doi.org/10.1016/j.seppur.2020.117691.
53. Wei, K.; Wang, B.; Hu, J.; Chen, F.; Hao, Q.; He, G.; Wang, Y.; Li, W.; Liu, J.; He, Q. Photocatalytic Properties of a New Z-Scheme System $BaTiO_3$/In_2S_3 with a Core-Shell Structure. *RSC Adv.* **2019**, *9*, 11377–11384. https://doi.org/10.1039/c8ra10592h.
54. Jiang, D.; Zhu, Y.; Chen, M.; Huang, B.; Zeng, G.; Huang, D.; Song, B.; Qin, L.; Wang, H.; Wei, W. Modified Crystal Structure and Improved Photocatalytic Activity of MIL-53 via Inorganic Acid Modulator. *Appl. Catal. B Environ.* **2019**, *255*, 117746. https://doi.org/10.1016/j.apcatb.2019.117746.
55. Gao, Z.; Yao, B.; Xu, T.; Ma, M. Effect and Study of Reducing Agent $NaBH_4$ on Bi/BiOBr/CdS Photocatalyst. *Mater. Lett.* **2020**, *259*, 126874. https://doi.org/10.1016/j.matlet.2019.126874.
56. Che, H.; Liu, C.; Hu, W.; Hu, H.; Li, J.; Dou, J.; Shi, W.; Li, C.; Dong, H. NGQD Active Sites as Effective Collectors of Charge Carriers for Improving the Photocatalytic Performance of Z-Scheme g-C_3N_4/Bi_2WO_6 Heterojunctions. *Catal. Sci. Technol.* **2018**, *8*, 622–631. https://doi.org/10.1039/c7cy01709j.
57. Hao, C. chen; Tang, Y. bin; Shi, W. long; Chen, F. yan; Guo, F. Facile Solvothermal Synthesis of a Z-Scheme 0D/3D CeO_2/$ZnIn_2S_4$ Heterojunction with Enhanced Photocatalytic Performance under Visible Light Irradiation. *Chem. Eng. J.* **2021**, *409*, 128168. https://doi.org/10.1016/j.cej.2020.128168.
58. Zhu, Z.; Xia, H.; Wu, R.; Cao, Y.; Li, H. Fabrication of La_2O_3/g-C_3N_4 Heterojunction with Enhanced Photocatalytic Performance of Tetracycline Hydrochloride. *Crystals* **2021**, *11*, 1349. https://doi.org/10.3390/cryst11111349.

59. Tian, Q.; Zhuang, J.; Wang, J.; Xie, L.; Liu, P. Novel Photocatalyst, $Bi_2Sn_2O_7$, for Photooxidation of As(III) under Visible-Light Irradiation. *Appl. Catal. A Gen.* **2012**, *425–426*, 74–78. https://doi.org/10.1016/j.apcata.2012.03.005.
60. Yaghoot-Nezhad, A.; Moradi, M.; Rostami, M.; Danaee, I.; Khosravi-Nikou, M.R. Dual Z-Scheme CuO-ZnO@Graphitic Carbon Nitride Ternary Nanocomposite with Improved Visible Light-Induced Catalytic Activity for Ultrasound-Assisted Photocatalytic Desulfurization. *Energy Fuels* **2020**, *34*, 13588–13605. https://doi.org/10.1021/acs.energyfuels.0c02012.